electronics

MDPI

Article

UAV Vulnerability to Lasers: Modeling and Experimental Assessment

Diogo Rocha [1,2], José Silvestre Silva [1,3,*], Daniel Silvestre [1,4,5], Joana Almeida [6], Dawei Liang [6] and Pedro Mendonça dos Santos [1,7]

1 Military Academy Research Center (CINAMIL), Portuguese Military Academy, 1169-203 Lisbon, Portugal; rocha.dmm@academiamilitar.pt (D.R.); dsilvestre@fct.unl.pt (D.S.); pms@lx.it.pt (P.M.d.S.)
2 Instituto Superior Técnico, Universidade de Lisboa, 1049-001 Lisbon, Portugal
3 Laboratory for Instrumentation, Biomedical Engineering and Radiation Physics (LIBPhys-UC, LA-REAL), Universidade de Coimbra, 3030-709 Coimbra, Portugal
4 Centre of Technology and Systems (CTS) & School of Science and Technology, Intelligent Systems Associate Laboratory (LASI), NOVA University of Lisbon (FCT/UNL), 2829-516 Caparica, Portugal
5 Institute for Systems and Robotics, Instituto Superior Técnico, University of Lisbon, 1049-001 Lisbon, Portugal
6 Centre of Physics and Technological Research (CEFITEC), Physics Department, NOVA School of Science and Technology, 2829-516 Caparica, Portugal; jla@fct.unl.pt (J.A.); dl@fct.unl.pt (D.L.)
7 Instituto de Telecomunicações, 1049-001 Lisbon, Portugal
* Correspondence: jose.silva@academiamilitar.pt

Abstract

Counter-unmanned aerial system technologies based on directed energy require a quantitative understanding of laser propagation and target vulnerability. This work presents a multiscale methodology for continuous-wave laser interaction with UAV components, combining a lumped-capacitance screening model, two three-dimensional thermal models, and an exploratory experimental campaign. The lumped campaign comprised 1350 laser–material–distance combinations and reached the prescribed threshold in 85.0% of cases. The three-dimensional campaigns comprised 160 additional cases. Acrylonitrile butadiene styrene (ABS) was selected as the representative structural target for the detailed three-dimensional analysis because the lumped screening identified it as one of the most thermally susceptible UAV materials, while also representing a typical polymeric fairing material. The ABS threshold was reached in 95.0% of the three-dimensional cases.For the experimental campaign, the PGL-V-H-1064 laser (Changchun New Industries Optoelectronics Technology Co., Ltd., Changchun, China) was selected as the available laboratory source. It operates at 1064 nm and its output power was experimentally measured to be approximately 1.0 W. Under the modeled conditions, the PGL-V-H-1064 laser crossed the ABS threshold only at 5 m, after 2.913 s, whereas the equivalent-camera functional threshold was not reached. Experimentally, the PGL-V-H-1064 laser produced reversible dazzling in all tested cameras. RunCam, BetaFPV, and Caddx Ratel 2 cameras showed no permanent damage, whereas a low-cost drone camera was permanently damaged after 120 s at 3 m. Localized damage was also observed on the drone fairing and propeller, with propeller degradation causing loss of flight stability. These results highlight the distinction between temporary optical disruption and permanent thermal or structural damage.

Keywords: counter-UAS; UAV; directed energy; laser; thermal modeling; CMOS camera; soft-kill; hard-kill; ABS; beam propagation

Check for updates

Academic Editors: Gennaro Ariante, Umberto Papa, Giuseppe Del Core and Salvatore Ponte

Received: 29 September 2026
Revised: 19 October 2026
Accepted: 23 October 2026
Published: 26 October 2026

Copyright: © 2026 by the authors. Licensee MDPI, Basel, Switzerland. This article is an open access article distributed under the terms and conditions of the Creative Commons Attribution (CC BY) license.

1. Introduction

The rapid dissemination of small unmanned aerial vehicles (UAVs) has increased the need for counter-unmanned aerial system (C-UAS) technologies capable of detecting, tracking, and neutralizing low-cost, maneuverable, and low-signature platforms. Conventional countermeasures include kinetic interception, radio-frequency interference, navigation-signal manipulation, high-power microwaves, and directed-energy systems [1]. Cyber and communication vulnerabilities further broaden this counter-UAS landscape: recent studies have reviewed attack vectors affecting commercial UAV communication and control systems [2] and proposed structured methods for assessing platform-level security and susceptibility to cyber-attacks [3]. Complementarily, experimental work has demonstrated that radio-frequency jamming and Global Navigation Satellite System (GNSS) spoofing can disrupt UAV communication and navigation functions, illustrating the practical relevance of non-kinetic approaches to drone neutralization [4]. Among these approaches, lasers offer highly localized energy delivery, low time of flight [5], and the possibility of acting selectively on optical, electronic, or structural subsystems [6].

Laser effects on UAVs can be divided conceptually into two classes. In a soft-kill interaction, the objective is to degrade a sensor or mission function without necessarily producing structural destruction. Optical cameras may exhibit temporary saturation, loss of contrast, blooming, or dazzling when sufficiently intense radiation reaches the image sensor [7–9]. Under more severe irradiation, permanent damage to the sensor, filters, microlenses, packaging, or associated electronics may occur. In a hard-kill interaction, absorbed laser energy produces thermal degradation of a structural, propulsion, control, or electronic component to the point that a critical function is lost [10–13].

The effectiveness of a laser cannot be inferred from nominal output power alone. Beam quality, initial beam diameter, divergence, wavelength, optical efficiency, atmospheric transmission, pointing stability, target distance, dwell time, and target absorption strongly influence the irradiance ultimately delivered to the illuminated region. Atmospheric turbulence and tracking errors can further reduce the effective dwell time and peak irradiance at the aimpoint [14–16]. Experimental studies have also shown that the time required to produce material degradation increases rapidly when beam expansion, imperfect focusing, or atmospheric effects reduce the energy density at the target [6].

Existing studies typically emphasize one part of this problem. Some focus on optical sensor dazzling and saturation [7,8]; others examine thermal damage to structural composites or flight-control electronics [11–13]; and others focus on acquisition, tracking, pointing, and atmospheric propagation [14,15]. Liu et al. additionally investigated the vulnerability of UAV propulsion components to laser irradiation, showing that component-level susceptibility and geometric exposure can strongly influence the resulting damage [17]. Although highly detailed models exist for selected components or engagement scenarios, direct comparison of multiple laser technologies, materials, distances, and cost assumptions under a common set of equations remains less common.

Recent studies illustrate this fragmentation more explicitly. Veerabuthiran et al. investigated the disruption of complementary metal-oxide-semiconductor (CMOS) sensors using a 1064 nm nanosecond pulsed laser, experimentally characterizing both sensor saturation and permanent damage [18]. However, their analysis was restricted to pulsed irradiation of an imaging sensor and did not consider continuous-wave exposure or structural UAV components. Song et al. examined continuous-wave laser damage in carbon-fiber-reinforced polymer (CFRP) laminates using experiments and thermo-mechanical simulations, focusing on ablation, heat-affected zones, and residual structural strength [19]. In parallel, Zhang et al. investigated laser-beam propagation under atmospheric turbulence, addressing propagation degradation rather than the subsequent thermal response of the target [20].

In contrast, the present work combines beam propagation, large-scale thermal screening, spatially resolved three-dimensional modeling of both structural and electro-optical targets, and exploratory continuous-wave experiments within a common framework.

The approach proposed here addresses this fragmentation through three complementary levels of thermal analysis. First, a lumped-capacitance model provides fast screening over a large parameter space. Second, a three-dimensional finite-difference model resolves spatial temperature gradients, hotspot formation, and depth-wise absorption in representative UAV materials. Third, a dedicated equivalent-camera model introduces an approximate wavelength-dependent coupling factor for a lens–IR-cut-filter–CMOS–substrate assembly. This separation is important because a structural polymer directly absorbing incident radiation is physically different from an electro-optical system in which the incident beam interacts with optical elements before reaching the sensor.

The numerical framework estimates laser energy deposition and the resulting thermal response but does not explicitly simulate optical sensor saturation or dazzling. Experimental observations were therefore used to distinguish reversible optical disruption from persistent functional degradation and structural damage.

Accordingly,the objectives of this study are to (i) develop a uniform framework for comparing continuous-wave lasers against representative UAV components; (ii) quantify the influence of distance, beam characteristics, wavelength-dependent absorption, and target properties on threshold time; (iii) compare global lumped predictions with spatially resolved three-dimensional results; (iv) examine the distinct thermal response of an acrylonitrile butadiene styrene (ABS) structural target and an equivalent UAV camera; and (v) experimentally assess reversible optical disruption, permanent camera damage, and localized structural damage using the PGL-V-H-1064 laser, operating at 1064 nm with an output power of 1.0 W.

The principal contribution of this study is the integration of complementary modeling approaches. In contrast to previous studies that have typically examined sensor dazzling, structural thermal damage, beam propagation, or individual UAV subsystems separately, the proposed approach combines large-scale laser–material–distance screening, spatially resolved three-dimensional thermal modeling of both structural and electro-optical targets, wavelength-dependent camera coupling, and exploratory continuous-wave experiments. This combined framework enables laser sources, target types, and engagement distances to be evaluated under common assumptions, while also distinguishing reversible optical soft-kill effects from permanent thermal or structural damage. Its practical value lies in providing a reproducible screening methodology for identifying the most relevant laser–target scenarios for subsequent detailed modeling and experimental investigation.

2. Materials and Methods

2.1. Methodological Framework

The methodology combines laser parametrization, Gaussian beam propagation, equivalent material properties, thermal threshold criteria, numerical verification, and comparative performance metrics. The laser source is first characterized by wavelength, nominal power, optical efficiency, beam-quality factor, and initial beam diameter. The beam is propagated to the target plane, where the delivered irradiance is coupled to a material or an equivalent camera. Thermal evolution is then solved either by a lumped-capacitance approximation or by an explicit three-dimensional finite-difference formulation.

The models predominantly consider continuous-wave irradiation because the study focuses on sustained heating over time scales ranging from milliseconds to seconds. By contrast, pulsed and ultrashort-pulse regimes require additional treatment of pulse energy, repetition rate, peak intensity, nonequilibrium electron–lattice dynamics, nonlinear ion-

ization, ablation, and laser-induced plasma formation. These interaction mechanisms are therefore outside the scope of the present thermal formulation [21,22].

2.2. Laser Parametrization and Beam Propagation

For each laser, the principal parameter set is

$$\mathcal{L} = \left\{ \lambda, P, \eta_{\text{opt}}, M^2, D_0 \right\}, \tag{1}$$

where λ is the wavelength, P is the source power, η_{opt} is the adopted global optical-efficiency factor, M^2 is the beam-quality factor, and D_0 is the initial beam diameter. The initial beam radius is

$$w_0 = \frac{D_0}{2}, \tag{2}$$

and the useful nominal power is

$$P_{\text{nom}} = P\eta_{\text{opt}}. \tag{3}$$

A Gaussian-beam approximation is used. The Rayleigh length is

$$z_R = \frac{\pi w_0^2}{M^2 \lambda}, \tag{4}$$

and the ideal beam radius at distance z is

$$w(z) = w_0 \sqrt{1 + \left(\frac{z}{z_R} \right)^2}. \tag{5}$$

In the three-dimensional models, atmospheric transmission is represented by a simplified Beer–Lambert relation,

$$T_{\text{atm}}(z) = \exp(-\beta_{\text{ext}} z), \tag{6}$$

giving

$$P_{\text{target}}(z) = P_{\text{nom}} T_{\text{atm}}(z). \tag{7}$$

Additional beam broadening is represented empirically by

$$w_{\text{eff}}(z) = w(z)(1 + k_{\text{turb}} z). \tag{8}$$

This expression is intentionally simplified and is not intended as a complete turbulence model.

The irradiance distribution at the target plane is

$$I(x, y, z) = I_0(z) \exp\left[-\frac{2(x^2 + y^2)}{w_{\text{eff}}^2(z)} \right], \tag{9}$$

with

$$I_0(z) = \frac{2P_{\text{target}}(z)}{\pi w_{\text{eff}}^2(z)}. \tag{10}$$

Normal incidence is assumed throughout the final simulation campaigns.

2.3. Equivalent UAV Targets and Spectral Absorption

Representative UAV components are modeled through equivalent thermal and optical properties,

$$\mathcal{M} = \{ \rho, c_p, k, h_m, \alpha_s, \mu, \varepsilon, h_{\text{conv}}, E_0, T_{\text{lim}} \}, \tag{11}$$

where ρ is density, c_p is specific heat, k is thermal conductivity, h_m is thickness, α_s is surface absorptivity, μ is the volumetric absorption coefficient, ε is emissivity, h_{conv} is the convection coefficient, E_0 is the initial elastic modulus when applicable, and T_{lim} is a thermal or functional threshold.

In the material-based three-dimensional model, the base absorption properties are modified through effective wavelength-band factors:

$$\alpha_s^*(\lambda, C_M) = \alpha_s F_\alpha(\lambda, C_M), \tag{12}$$

$$\mu^*(\lambda, C_M) = \mu F_\mu(\lambda, C_M), \tag{13}$$

where C_M identifies the material class. These factors are approximate sensitivity coefficients rather than experimentally measured spectral curves. Their purpose is to avoid treating blue, green, 808 nm, and 1064–1070 nm irradiation as thermally equivalent for every target material.

2.4. Lumped-Capacitance Thermal Model

The lumped model assumes a spatially uniform temperature,

$$T = T(t). \tag{14}$$

The effective illuminated area is

$$A_{\text{eff}}(z) = \frac{\pi w^2(z)}{2}, \tag{15}$$

and the corresponding effective volume and mass are

$$V = A_{\text{eff}} h_m, \qquad m = \rho A_{\text{eff}} h_m. \tag{16}$$

The fraction of energy absorbed through the material thickness is represented by

$$\eta_{\text{prof}} = 1 - \exp(-\mu h_m). \tag{17}$$

The absorbed laser power is

$$P_{\text{abs}} = I_{\text{med}} A_{\text{eff}} \alpha_s \eta_{\text{prof}}, \tag{18}$$

where $I_{\text{med}} = 2P_{\text{nom}}/(\pi w^2)$ under the lumped formulation.

Convective and radiative losses are

$$Q_{\text{conv}} = h_{\text{conv}} A_{\text{loss}} (T - T_{\text{amb}}), \tag{19}$$

$$Q_{\text{rad}} = \varepsilon \sigma_{\text{SB}} A_{\text{loss}} \left(T^4 - T_{\text{amb}}^4 \right), \tag{20}$$

with $A_{\text{loss}} \approx 2A_{\text{eff}}$. The energy balance is

$$m c_p \frac{dT}{dt} = P_{\text{abs}} - Q_{\text{conv}} - Q_{\text{rad}}. \tag{21}$$

It is integrated explicitly as

$$T^{n+1} = T^n + \frac{\left(P_{\text{abs}}^n - Q_{\text{conv}}^n - Q_{\text{rad}}^n \right) \Delta t}{m c_p}. \tag{22}$$

The threshold time is defined as

$$t_{\text{lim}} = \min\{t : T(t) \geq T_{\text{lim}}\}. \tag{23}$$

When the crossing occurs between two integration steps, linear interpolation is used. The Biot number,

$$Bi = \frac{h_{\text{conv}} L_c}{k}, \tag{24}$$

is used only as a diagnostic for the appropriateness of the lumped approximation [23,24].

2.5. Three-Dimensional Thermal Model for UAV Materials

The spatial model solves

$$T = T(x, y, z, t) \tag{25}$$

within a rectangular domain. The depth is equal to the material thickness,

$$L_z = h_m, \tag{26}$$

whereas the lateral dimensions are selected as

$$L_x = L_y = \max(6w_{\text{eff}}, L_{\text{min}}). \tag{27}$$

For a uniform grid with N_x, N_y, and N_z nodes, the temperature field is advanced using the heat equation

$$\frac{\partial T}{\partial t} = \alpha \nabla^2 T + \frac{q'''(x, y, z)}{\rho c_p}, \qquad \alpha = \frac{k}{\rho c_p}. \tag{28}$$

Depth-wise absorption is represented layer by layer. For each depth cell,

$$f_k = \exp(-\mu^* z_{k-1/2}) - \exp(-\mu^* z_{k+1/2}), \tag{29}$$

and the volumetric heat source is

$$q'''_{i,j,k} = \alpha_s^* I(x_i, y_j, z) \frac{\exp(-\mu^* z_{k-1/2}) - \exp(-\mu^* z_{k+1/2})}{\Delta z}. \tag{30}$$

Central finite differences are used for the Laplacian in the interior of the domain. Surface convection and radiation are applied explicitly after conduction and source deposition:

$$q''_{\text{loss}} = h_{\text{conv}}(T_s - T_{\text{amb}}) + \varepsilon \sigma_{\text{SB}} \left(T_s^4 - T_{\text{amb}}^4 \right). \tag{31}$$

The explicit time step is restricted by

$$\Delta t = \min \left[\Delta t_{\text{req}}, \frac{0.45}{2\alpha(\Delta x^{-2} + \Delta y^{-2} + \Delta z^{-2})} \right]. \tag{32}$$

The principal outputs are maximum temperature, domain-average temperature, threshold time, and the numerical fraction of the mesh above the threshold:

$$f_{\text{lim}}(t) = \frac{N[T_{i,j,k}(t) \geq T_{\text{lim}}]}{N_x N_y N_z}. \tag{33}$$

This fraction is a numerical-domain metric and must not be interpreted as the physical percentage of a component that has been destroyed.

2.6. Equivalent Camera Model

The camera is represented as a homogeneous thermal equivalent of an optical lens, IR-cut filter, CMOS sensor, and electronic substrate. The equivalent thickness is

$$h_{\mathrm{cam}} = \sum_i h_i, \tag{34}$$

with density and specific heat obtained by thickness- and mass-weighted averaging. The effective through-thickness conductivity is approximated through a harmonic mean.

The resulting equivalent camera had a total thickness of 2.45 mm, an effective density of 2210.41 $\mathrm{kg\,m^{-3}}$, a specific heat of 862.03 $\mathrm{J\,kg^{-1}\,K^{-1}}$, and an effective through-thickness thermal conductivity of 0.565 $\mathrm{W\,m^{-1}\,K^{-1}}$. The adopted emissivity and convective heat-transfer coefficient were 0.85 and 12 $\mathrm{W\,m^{-2}\,K^{-1}}$, respectively. These values represent the global thermal equivalent of the lens–IR-cut-filter–CMOS-sensor–electronic-substrate assembly and should not be interpreted as the properties of any individual layer.

Because measured transmission curves for the actual cameras were not available in the numerical phase, the model uses a band-dependent effective coupling factor $F_{\mathrm{cam}}(\lambda)$. The power coupled to the equivalent camera is

$$P_{\mathrm{cam}}(z,\lambda) = P_{\mathrm{nom}}\,T_{\mathrm{atm}}(z)\,F_{\mathrm{cam}}(\lambda). \tag{35}$$

The spectral factors used in the numerical campaign are summarized in Table 1. Since manufacturer-specific spectral transmission curves for the lenses and IR-cut filters, together with sensor responsivity curves, were not available for the cameras considered, the adopted values were not obtained by fitting or calibrating the model to a particular device. Instead, they were selected as band-specific engineering estimates intended to represent plausible qualitative trends of the complete optical stack. Relatively high effective coupling was assigned in the visible range, an intermediate value was adopted at 808 nm, and a lower value was used in the 1064–1070 nm band. This qualitative ordering is consistent with the wavelength-dependent response reported for CMOS imaging systems and with the reduced near-infrared absorption of conventional silicon detectors as the wavelength approaches 1064 nm. The adopted values of $F_{\mathrm{cam}} = 0.80$, 0.30, and 0.10 should therefore be interpreted as representative sensitivity parameters rather than measured transmission coefficients. The corresponding values of α_s and μ were assigned consistently with the same assumed spectral ordering. Because reliable device-specific spectral data were not available for the cameras considered in this study, the numerical camera results should be interpreted as sensitivity-based predictions rather than calibrated responses of a specific commercial camera.

Table 1. Assumed effective spectral parameters adopted for the equivalent camera model.

Spectral Band	F_{cam}	α_s	μ [$\mathrm{m^{-1}}$]
Visible blue	0.80	0.55	2.5×10^4
Visible green	0.80	0.50	2.0×10^4
Near infrared, 808 nm	0.30	0.40	1.5×10^4
Near infrared, 1064–1070 nm	0.10	0.30	1.0×10^4

To quantify the influence of the assumed optical parameters on the predicted camera response, a one-at-a-time sensitivity analysis was performed for the 1064–1070 nm band. The effective camera coupling factor F_{cam}, the surface absorptivity α_s, and the volumetric absorption coefficient μ were independently varied by ±25% relative to their nominal

values, while all remaining model parameters were kept unchanged. Two representative cases were considered: the 1 W PGL-V-H-1064 source at 5 m, representing a non-threshold case, and the 5 kW Fiber IPG YLS source at 100 m, representing a threshold-crossing case. The analysis was used to evaluate the sensitivity of the maximum temperature and threshold time to prescribed ±25% variations in the assumed optical parameters.

The model does not explicitly resolve internal optical focusing, interfacial reflections, microlenses, pixel-level photocarrier generation, sensor saturation, automatic exposure control, blooming, or recovery after exposure. Therefore, a thermal threshold in this model is interpreted as a possible functional thermal limit and not as a direct prediction of optical dazzling.

2.7. Thermal and Functional Criteria

Three effect levels are distinguished: (i) optical disruption, including dazzling, saturation, blooming, and loss of contrast; (ii) thermally induced functional degradation; and (iii) irreversible physical damage such as severe deformation, carbonization, delamination, melting, ablation, or destruction of a critical component.

For the three-dimensional model, the threshold is applied locally:

$$t_{\mathrm{lim,3D}} = \min\left\{ t : \max_{i,j,k} T_{i,j,k}(t) \geq T_{\mathrm{lim}} \right\}. \tag{36}$$

The thermal and functional thresholds adopted in this study do not represent a single physical failure mechanism. Instead, they are target-specific screening criteria selected to identify the onset of a physically relevant thermal regime for each material or component. Consequently, crossing T_{lim} should not be interpreted uniformly as complete destruction or permanent functional failure. Some thresholds are directly associated with well-established material transitions, whereas others are engineering criteria used for comparative screening when a universal failure temperature does not exist. Table 2 summarizes the physical meaning and basis assigned to each threshold used in the numerical campaign.

Table 2. Physical interpretation and basis of the thermal and functional thresholds adopted in the numerical models.

Target/Material	T_{lim} [K]	Physical Interpretation and Basis
ABS fairing	373.15	Approximate onset of the glass-transition/softening regime. Reported ABS glass-transition temperatures are approximately 100–110 °C [25]. The criterion therefore indicates increasing susceptibility to softening, deformation, and stiffness loss, rather than melting or complete structural destruction.
Polycarbonate fairing	423.15	Representative glass-transition/softening criterion. Commercial polycarbonate grades report glass-transition temperatures close to 145 °C and Vicat softening temperatures around 144–147 °C [26]. The adopted 150 °C criterion therefore represents substantial softening rather than complete material destruction.
Glass-fiber-reinforced nylon	443.15	Assumed high-temperature matrix-deformation screening criterion for the polymer matrix. The precise response depends strongly on nylon grade, fiber fraction, moisture content, and processing history; therefore, this value is used for comparative screening and is not interpreted as a universal glass-transition, melting, or failure temperature.
CFRP structural arm	450.15	Engineering matrix-softening/degradation criterion. It represents a temperature at which significant degradation of the polymer matrix and loss of composite structural performance may become relevant; it does not imply failure or melting of the carbon fibers themselves.
Aluminum structure	933.15	Approximate melting-point criterion, corresponding to about 660 °C. Crossing this threshold represents a severe thermal condition associated with loss of structural integrity rather than the onset of minor thermal degradation.
Magnesium structure	923.15	Approximate melting-point criterion, corresponding to about 650 °C. It represents a severe thermal condition associated with loss of structural integrity.
Stainless-steel shaft	1700.15	Representative high-temperature melting/softening criterion within the melting range of common stainless-steel grades. The exact transition depends on alloy composition and should therefore be regarded as an approximate screening limit.

Table 2. *Cont.*

Target/Material	T_{lim} [K]	Physical Interpretation and Basis
FR4 electronic board	403.15	Approximate glass-transition criterion for a conventional lower-T_g glass-fiber/epoxy laminate. Commercial FR4 laminates are available with T_g values around 130 °C [27]. Crossing this threshold indicates substantial matrix softening and reduced dimensional or mechanical stability rather than destruction of the complete electronic board.
Silicon sensor	398.15	Conservative high-temperature screening criterion for the idealized sensor target. The value corresponds to 125 °C, which is comparable to upper storage temperature ratings reported for some CMOS image sensors [28]. It is not a silicon melting temperature, a normal operating limit, or a universal CMOS permanent-damage threshold.
Optical-glass lens	820.15	Representative glass-transformation/deformation criterion. SCHOTT N-BK7 optical glass, for example, has a reported transformation temperature of approximately 557 °C [29]. The adopted screening threshold was set at 547 °C, 10 °C below the reported transformation temperature, to provide a conservative reference criterion. It is therefore used as an approximate high-temperature optical-glass screening threshold rather than as a universal lens-failure temperature.
Equivalent camera	358.15	Functional thermal criterion for the complete lens–filter–sensor–electronics equivalent. The value corresponds to 85 °C, which is representative of the upper operating-temperature limit reported for some commercial CMOS image sensors [30]. It is therefore a functional screening limit and not a universal permanent-damage temperature for CMOS cameras.

2.8. Simulation Campaigns and Performance Metrics

The final lumped campaign consisted of 15 continuous-wave lasers, 10 representative materials, and nine target distances, totaling 1350 scenarios. The three-dimensional study added the PGL-V-H-1064 laser (1064 nm, 1.0 W) to the 15-system set and evaluated five distances, giving 80 ABS cases and 80 equivalent-camera cases. The main parameters of the numerical campaigns are summarized in Table 3.

Table 3. Summary of the numerical campaigns.

Parameter	Lumped Model	3D ABS	3D Camera
Laser systems	15	16	16
Target types	10 materials/components	ABS	Equivalent camera
Distances [m]	5, 10, 25, 50, 60, 70, 80, 90, 100	5, 10, 25, 50, 100	5, 10, 25, 50, 100
Maximum exposure	5 s	120 s	120 s
Maximum requested time step	10^{-3} s	10^{-3} s	10^{-3} s
Grid	–	$41 \times 41 \times 21$	$41 \times 41 \times 21$
Atmosphere	not explicit	clean air	clean air
Threshold	material-dependent	373.15 K	358.15 K
Number of scenarios	1350	80	80

The threshold success rate is

$$R_{\text{lim}} = \frac{N_{\text{lim}}}{N_{\text{total}}} \times 100\%. \tag{37}$$

For cases in which the prescribed threshold was reached, threshold times were summarized using the median. To provide only a preliminary source-cost comparison, the following source-cost proxy is defined:

$$J_i = C_{L,i} t_{\text{lim},i}, \tag{38}$$

where C_L is the estimated acquisition price of the laser source. The ranking gives priority to success rate and uses the median J only as a secondary criterion among systems with equal success rates. The quantity J is not a complete cost-effectiveness metric and does

not represent total C-UAS system cost. It excludes, among other items, acquisition and tracking sensors, beam-delivery optics, cooling, power supply, stabilization, integration, maintenance, training, and operating costs.

2.9. Exploratory Experimental Assessment

An exploratory experimental campaign was performed as a qualitative complement to the numerical analysis and to distinguish temporary optical disruption from permanent camera or structural damage. The experimental campaign was not designed as a direct quantitative comparison with the numerical predictions because the numerical and experimental conditions were not matched on a point-by-point basis. In particular, the laser–target distances and irradiation conditions differed between the two parts of the study. Consequently, the numerical and experimental results are compared only in terms of qualitative trends, response mechanisms, and observed effects. The campaign used the PGL-V-H-1064 laser, operating at 1064 nm, with an output power of 1.0 W.

The numerical and experimental campaigns were not intended to reproduce identical irradiation conditions. The simulations included laser systems with substantially higher nominal powers than the source available for the laboratory tests, whereas the experimental campaign was constrained to the PGL-V-H-1064 laser. During the initial camera tests, corresponding to exposure durations between 30 and 90 s, the individual FPV cameras mainly exhibited reversible optical perturbation, with no observable permanent damage after removal of the beam. Consequently, extended exposures of 120 s were subsequently investigated to determine whether the increased cumulative thermal load delivered by the available low-power source could produce observable permanent effects. This approach should not be interpreted as implying that a long exposure to a low-power laser is quantitatively equivalent to a short exposure to a higher-power source. The thermal response also depends on irradiance, beam size, wavelength-dependent coupling, heat losses, and target properties. Rather, the extended exposures were used as an exploratory means of probing the effects of greater cumulative energy deposition with the laboratory hardware available, while the numerical models were used to examine conditions associated with substantially higher delivered power.

The optical targets comprised three individual cameras used in first-person-view systems—RunCam, BetaFPV, and Caddx Ratel 2—and the camera integrated in a low-cost commercial drone acquired specifically for the tests. Structural tests were also performed on components of the same drone, including the fairing and propeller.

Laser–target distances ranged from 0.5 to 6 m and exposure durations ranged from 5 to 120 s across the complete experimental campaign. The individual cameras were first irradiated with their lenses installed. Selected tests were subsequently repeated with the optical assembly removed and the sensor exposed directly to the incident beam. These additional tests were performed to assess the influence of the optical assembly on the laser–sensor interaction and to determine whether the absence of permanent damage observed with the lens installed could be associated with reflection, scattering, or attenuation of the 1064 nm radiation before reaching the photosensitive region. Direct sensor exposure therefore provided an additional condition for evaluating the susceptibility of the sensor in the absence of the intervening optical elements. During camera tests, the video signal was monitored during and after irradiation to distinguish temporary image perturbation, recovery, and permanent loss of function.

The exploratory campaign did not include a systematic set of replicate tests performed under identical irradiation conditions. Selected camera tests were repeated after removal of the optical assembly; however, these tests represent a different experimental configuration rather than statistical replicates of the lens-installed condition. Consequently, the

experimental observations are reported qualitatively and are not accompanied by statistical uncertainty measures, confidence intervals, or repeatability estimates.

For structural targets, the irradiated region was visually inspected after exposure and the drone was subsequently evaluated for observable functional consequences. The experimental outcomes were classified qualitatively as no permanent damage, partial/localized damage, or permanent damage. For camera tests, the occurrence of dazzling or temporary saturation was additionally recorded.

The experimental setup is shown in Figure 1.

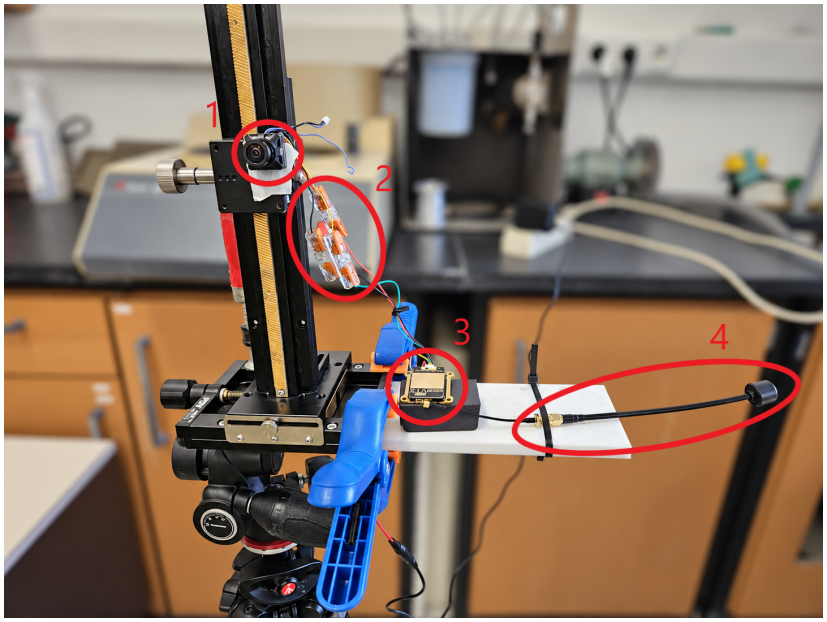


Figure 1. Experimental setup used for the laser irradiation tests. The main components of the setup are identified as follows: (**1**) FPV camera under test; (**2**) power and video wiring; (**3**) GEPRC RAD 5.8G 1.6 W video transmitter (Shenzhen Beizao Innovation Technology Co., Ltd., Shenzhen, China); (**4**) Pilotix Lollipop 5.8G SMA RHCP 160 mm antenna (Pilotix, Prague, Czech Republic).

The campaign was exploratory and was intended to provide qualitative experimental observations that can be compared with the numerical trends rather than a point-by-point comparison with the model predictions. The incident power at the target, actual beam diameter, irradiance, temperature during exposure, and spatial energy distribution were not directly measured, and beam alignment was adjusted manually. Therefore, the experimental observations are used only for qualitative comparison with the numerical results and not as a calibration dataset for the thermal models.

3. Results

3.1. Lumped-Model Numerical Verification

The prescribed thermal or functional threshold was reached in 1148 of 1350 lumped scenarios, corresponding to 85.0% of the campaign. The maximum relative energy-balance residual was approximately 1.55×10^{-11}%, indicating arithmetic consistency between absorbed, stored, and lost energy. This check does not constitute physical validation because the result still depends on the adopted material properties and modeling assumptions.

Temporal-independence tests were performed at maximum requested time steps of 10^{-3}, 5×10^{-4}, and 2.5×10^{-4} s for three representative cases. Maximum relative differences in threshold time were below 0.002%, so 10^{-3} s was retained as a compromise between numerical precision and computational cost. Nine of ten materials yielded $Bi < 0.1$; ABS

was the exception, with $Bi = 0.167$, reinforcing the interpretation of the lumped ABS results as screening estimates rather than a detailed local temperature prediction.

3.2. Influence of Distance

For the Fiber IPG YLR 1 kW laser applied to ABS, the lumped threshold time increased monotonically with distance: approximately 0.00653 s at 5 m, 0.04344 s at 50 m, and 0.15549 s at 100 m. The trend reflects beam expansion and, in the lumped formulation, the increase in effective heated mass as the illuminated area increases. This distance-dependent behavior is illustrated in Figure 2.

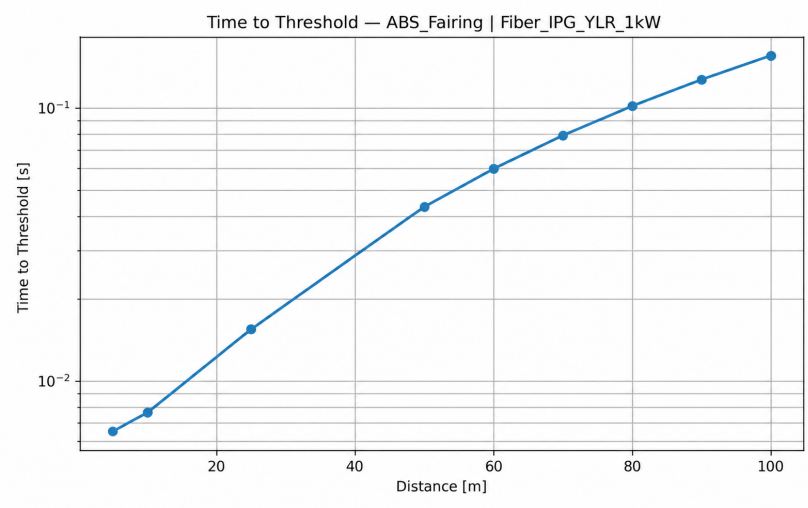


Figure 2. Threshold time for the ABS target as a function of laser–target distance for the Fiber IPG YLR 1 kW laser in the lumped model.

A broader comparison of the fraction of scenarios in which each laser system reached the prescribed thermal or functional threshold is presented in Figure 3.

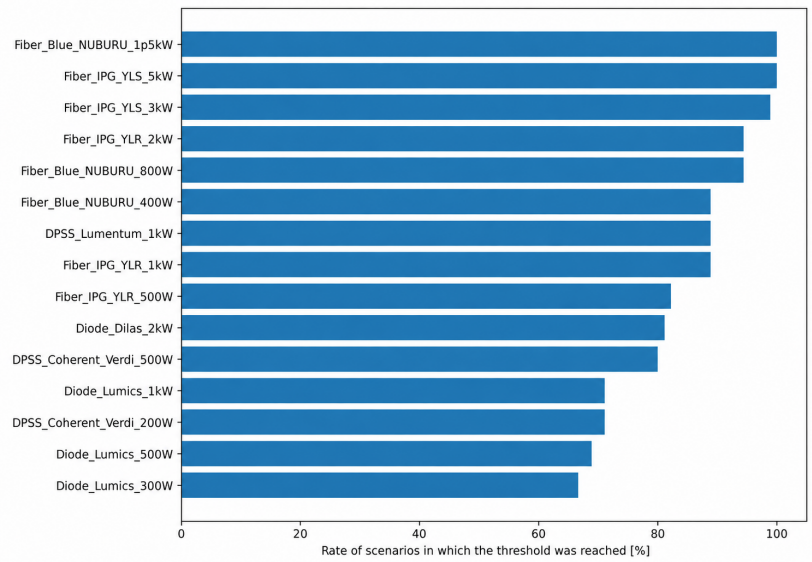


Figure 3. Fraction of scenarios in which the prescribed thermal or functional threshold was reached by each laser system in the lumped campaign.

3.3. Relative Vulnerability of Representative UAV Materials

Table 4 summarizes the success rate and median threshold time obtained for the ten representative targets in the lumped campaign. The silicon sensor exhibited the shortest

median time, whereas optical glass and metallic targets were less frequently driven above their adopted thresholds during the 5 s exposure window.

Table 4. Threshold crossing rate and median threshold time for representative UAV targets in the lumped campaign.

Component or Material	Threshold Reached [%]	Median t_{lim} [s]
Silicon sensor	100.0	0.0201
ABS fairing	100.0	0.0599
FR4 electronic board	100.0	0.0643
Polycarbonate fairing	100.0	0.0794
Glass-fiber-reinforced nylon	100.0	0.1325
CFRP structural arm	99.3	0.2031
Magnesium structure	80.7	0.6931
Aluminum structure	74.8	0.9751
Optical-glass lens	54.8	1.6392
Stainless-steel shaft	40.7	1.8690

The very short silicon threshold times should not be interpreted as destruction times for a real CMOS camera. They arise from an idealized equivalent volume with small thickness and a relatively low functional threshold. This distinction motivates the dedicated camera formulation used in the three-dimensional analysis.

3.4. Global Laser Performance and Preliminary Source-Cost Comparison

The Fiber IPG YLS 5 kW and Fiber Blue NUBURU 1.5 kW systems reached the prescribed threshold in all 90 scenarios associated with each laser. The Fiber IPG YLS 3 kW followed with a 98.9% success rate. The 300 W Diode Lumics system reached the threshold in 66.7% of its cases. These differences reflect the combined influence of useful power and beam concentration. The resulting preliminary source-cost ranking is summarized in Table 5.

Table 5. Preliminary source-cost ranking from the lumped screening campaign. Threshold success rate is the primary criterion; the median source-cost proxy J is used only as a secondary criterion.

Rank	Laser	Success [%]	Median t_{lim} [s]	Median Source-Cost Proxy J [EUR s]
1	Fiber IPG YLS 5 kW	100.0	0.0375	9755
2	Fiber Blue NUBURU 1.5 kW	100.0	0.0520	10,135
3	Fiber IPG YLS 3 kW	98.9	0.0552	9115
4	Fiber Blue NUBURU 800 W	94.4	0.0806	9269
5	Fiber IPG YLR 2 kW	94.4	0.0796	9549
6	Fiber Blue NUBURU 400 W	88.9	0.1466	9091
7	Fiber IPG YLR 1 kW	88.9	0.1352	9737
8	DPSS Lumentum 1 kW	88.9	0.1402	23,140
9	Fiber IPG YLR 500 W	82.2	0.2243	8523
10	Diode DILAS 2 kW	81.1	0.2310	12,010
11	DPSS Coherent Verdi 500 W	80.0	0.2335	22,180
12	Diode Lumics 1 kW	71.1	0.3616	11,571
13	DPSS Coherent Verdi 200 W	71.1	0.5463	26,220
14	Diode Lumics 500 W	68.9	0.5459	10,917
15	Diode Lumics 300 W	66.7	0.8502	11,903

The ranking is scenario-dependent and should not be interpreted as a universal ordering of laser technologies or as a complete cost-effectiveness analysis. It depends on the 5 s exposure window, the selected targets and thresholds, and the estimated laser-source acquisition prices. It is therefore presented only as a preliminary source-cost comparison under the assumptions of the screening campaign.

3.5. Numerical Three-Dimensional Response of ABS

The following three-dimensional results are exclusively numerical predictions and should not be interpreted as experimental measurements. The PGL-V-H-1064 laser was included in the numerical campaign to provide a reference case corresponding to the laser subsequently available for the experimental assessment. Its inclusion was therefore determined by laboratory availability rather than by an optimization or selection process among the simulated laser systems. Furthermore, the numerical distances considered for this source (5, 10, 25, 50, and 100 m) differ from the distances used during the experimental campaign (0.5–6 m). Consequently, the numerical and experimental PGL results are discussed separately and are compared only qualitatively.

The ABS threshold of 373.15 K was reached in 76 of 80 numerical three-dimensional cases, corresponding to 95.0%. Within the numerical campaign, the PGL-V-H-1064 source was simulated at distances of 5, 10, 25, 50, and 100 m. The four non-threshold cases corresponded to 10, 25, 50, and 100 m, whereas the simulated 5 m case crossed the threshold after approximately 2.913 s. These values are model predictions and do not correspond to the experimental irradiation conditions described in Section 2.9. The corresponding numerical results are summarized in Table 6.

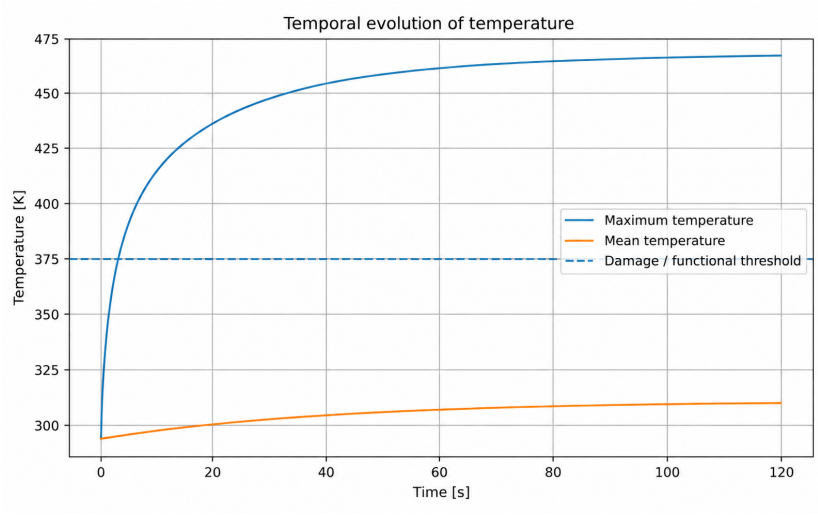
Table 6. Numerically predicted three-dimensional ABS response for the 1.0 W PGL-V-H-1064 laser at the simulated laser–target distances.

Distance [m]	T_{max} [K]	$\overline{T}$ [K]	t_{lim} [s]	f_{lim} [%]
5	466.71	309.56	2.913	2.73
10	367.98	297.74	–	0.00
25	311.19	293.91	–	0.00
50	298.19	293.34	–	0.00
100	294.44	293.20	–	0.00

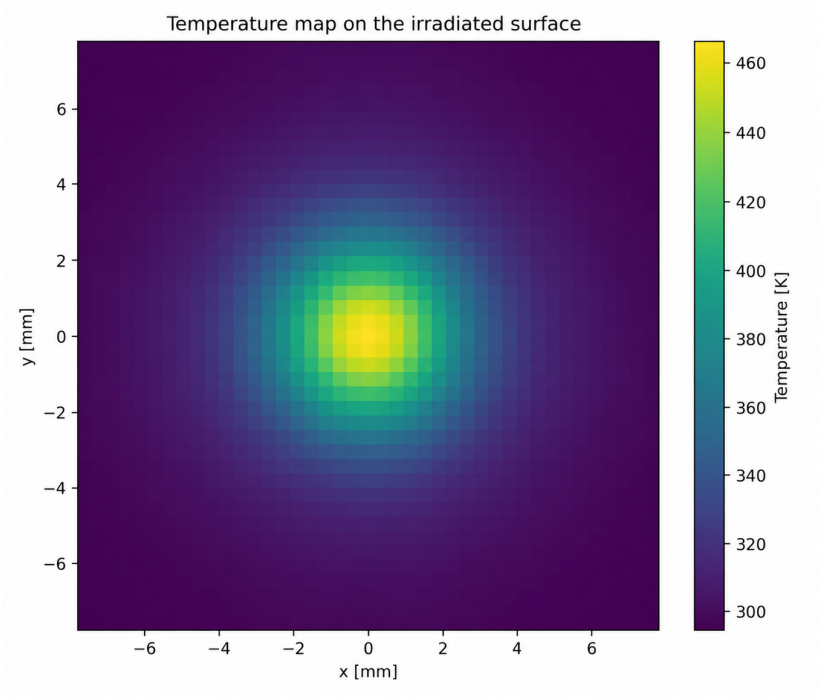
The strong difference between maximum and average temperatures indicates that the laser-induced heating was highly localized. At 5 m, the hotspot exceeded the adopted 373.15 K threshold while most of the numerical domain remained substantially cooler. This behaviour is also reflected by the relatively small fraction of the numerical mesh above the threshold, which reached only 2.73% at the end of the simulated exposure. The spatial response therefore cannot be represented adequately by a uniform target temperature when the laser beam remains concentrated over a small region.

The corresponding temporal evolution and surface temperature distribution are shown in Figure 4. The temperature decreased rapidly away from the beam centre, consistent with the Gaussian irradiance profile adopted in the model and with subsequent heat redistribution through conduction.

At longer ranges, substantially higher laser powers were required to produce rapid threshold crossing. For example, at 100 m, the Diode Lumics 300 W, Fiber IPG YLS 5 kW, and Fiber Blue NUBURU 1.5 kW systems reached the ABS threshold after 0.274 s, 0.005 s, and 0.003 s, respectively. These representative ABS cases are subsequently compared with the corresponding equivalent-camera results in Section 3.8.



(**a**) Temporal temperature evolution.



(**b**) Surface temperature map.

Figure 4. Numerically predicted response of the ABS fairing for the simulated PGL-V-H-1064 laser at 5 m: (**a**) maximum and average temperature as a function of time, together with the adopted thermal threshold; (**b**) surface temperature distribution in the x–y plane, expressed in kelvin.

The very high terminal temperatures predicted for some of these cases should not be interpreted as physically realistic temperatures of an intact ABS component. They result from continuing the constant-property thermal model after the material has exceeded the temperature range over which the adopted properties and geometry remain representative. For these severe irradiation conditions, the threshold-crossing time is therefore a more physically meaningful indicator than the final simulated temperature.

3.6. Numerical Three-Dimensional Response of the Equivalent Camera

The equivalent-camera threshold of 358.15 K was reached in 75 of 80 numerical three-dimensional scenarios, corresponding to 93.75%. The five non-threshold cases were

obtained for the simulated PGL-V-H-1064 laser at 5, 10, 25, 50, and 100 m. This numerical behaviour results from the combination of the comparatively low source power and the adopted effective coupling factor of 0.10 in the 1064–1070 nm band. These simulations are independent of the subsequent experimental tests and should not be interpreted as measurements performed at these distances. The corresponding numerical equivalent-camera results are summarized in Table 7.

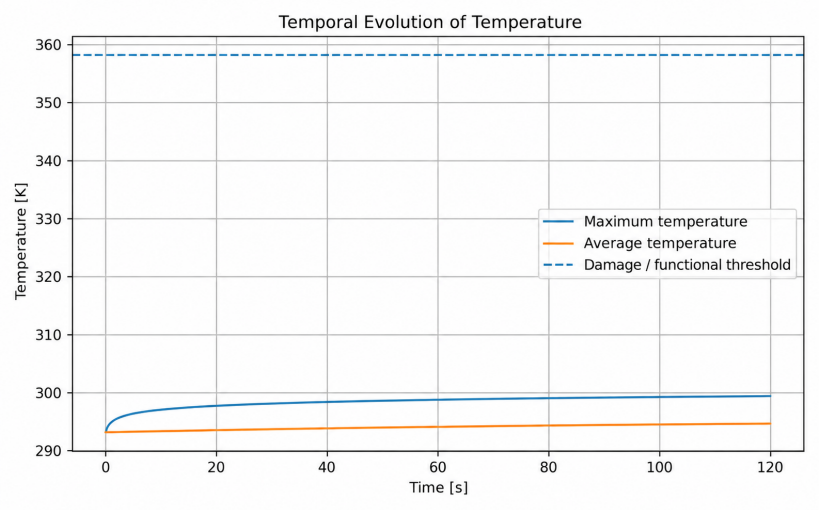
Table 7. Numerically predicted three-dimensional equivalent-camera response for the PGL-V-H-1064 laser (1.0 W) at the simulated laser–target distances.

Distance [m]	T_{max} [K]	$\overline{T}$ [K]	t_{lim} [s]	f_{lim} [%]
5	299.39	294.63	–	0.00
10	296.37	293.56	–	0.00
25	294.25	293.22	–	0.00
50	293.52	293.17	–	0.00
100	293.25	293.15	–	0.00

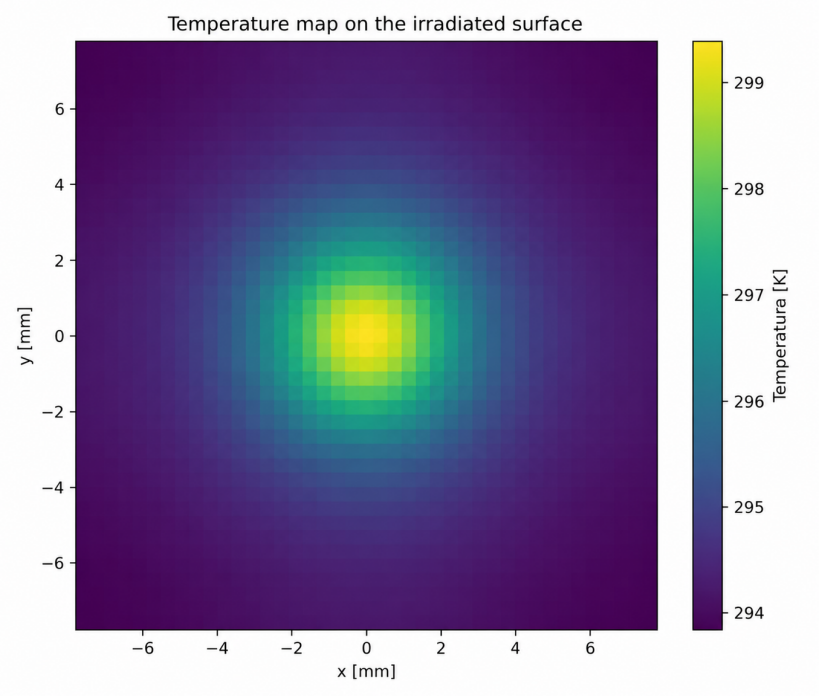
At 5 m, the adopted effective coupling factor of $F_{cam} = 0.10$ in the 1064–1070 nm band means that approximately 10% of the laser power transmitted through the atmosphere is coupled to the equivalent-camera thermal model. For the 1.0 W PGL-V-H-1064 laser, this corresponds to a coupled power slightly below 0.10 W after accounting for atmospheric transmission. Under the adopted thermal properties and boundary conditions, this coupled power was insufficient to drive the modeled temperature toward the 358.15 K functional threshold during the simulated exposure. Consequently, none of the PGL-V-H-1064 equivalent-camera cases reached the prescribed threshold, including the shortest simulated distance of 5 m. This result highlights the importance of distinguishing the nominal laser output power from the fraction of power that is effectively coupled to the modeled target, particularly when wavelength-dependent optical transmission and sensor coupling are considered.

The absence of threshold crossing in the equivalent-camera thermal model should not be interpreted as evidence that the camera is unaffected by the incident radiation. The adopted formulation represents only the thermal response associated with the effective absorbed power and does not explicitly simulate optical phenomena such as sensor saturation, blooming, loss of contrast, or dazzling. These effects may occur at irradiance levels below those required to produce the prescribed thermal functional threshold and were therefore assessed separately during the experimental campaign. Accordingly, the numerical PGL-V-H-1064 result should be interpreted as indicating that the adopted thermal criterion was not reached, rather than as demonstrating the absence of temporary optical disruption.

The higher-power representative equivalent-camera cases are subsequently compared with the corresponding ABS results in Section 3.8. Despite its lower nominal power, the 1.5 kW blue system crossed the equivalent-camera threshold much faster than the 5 kW near-infrared system in the adopted model. This behavior results from the combined effect of stronger effective spectral coupling and favorable beam concentration, showing that nominal laser power alone is insufficient to characterize the thermal response of an optical target. Wavelength-dependent coupling, atmospheric transmission, beam spreading, and the target-specific interaction model must therefore be considered together when interpreting the predicted threshold times. The numerical response of the equivalent-camera model for the PGL-V-H-1064 laser at 5 m is shown in Figure 5.



(**a**) Temporal temperature evolution.



(**b**) Surface temperature map.

Figure 5. Numerically predicted response of the equivalent-camera model for the simulated PGL-V-H-1064 laser (Changchun New Industries Optoelectronics Technology Co., Ltd., Changchun, China) at 5 m: (**a**) maximum and average temperature as a function of time, together with the adopted functional thermal threshold; (**b**) surface temperature distribution in the x–y plane, expressed in kelvin.

3.7. Sensitivity to Equivalent-Camera Optical Parameters

A one-at-a-time sensitivity analysis was performed to quantify the influence of the assumed equivalent-camera optical parameters on the predicted thermal response. The effective camera coupling factor F_{cam}, the surface absorptivity α_s, and the volumetric absorption coefficient μ were independently varied by $\pm 25\%$ relative to their nominal values, while all remaining model parameters were kept unchanged. Two representative cases in the 1064–1070 nm band were considered: the PGL-V-H-1064 laser at 0.8 W and 5 m, representing a non-threshold case, and the 5 kW Fiber IPG YLS source at 100 m, representing a threshold-crossing case. The analysis therefore assesses the sensitivity of

both the predicted maximum temperature and threshold time to plausible variations in the assumed optical parameters. The results are summarized in Table 8.

Table 8. Sensitivity of the equivalent-camera model to ±25% variations in the assumed optical parameters. Each parameter was varied independently while all remaining parameters were kept at their nominal values.

Case and Parameter	−25%	Nominal	+25%
PGL 0.8 W, 5 m – T_{max} [K]			
F_{cam}	297.83	299.39	300.95
α_s	297.83	299.39	300.95
μ	299.29	299.39	299.46
Fiber IPG YLS 5 kW, 100 m – t_{lim} [s]			
F_{cam}	0.148	0.104	0.080
α_s	0.148	0.104	0.080
μ	0.121	0.104	0.093

For the two representative cases investigated, the predicted equivalent-camera response was more sensitive to F_{cam} and α_s than by μ. For the PGL-V-H-1064 case at 1 W and 5 m, decreasing either F_{cam} or α_s by 25% reduced T_{max} from 299.39 to 297.83 K, whereas increasing either parameter by 25% increased T_{max} to 300.95 K. In contrast, varying μ over the same relative range produced only a small change in T_{max}, from 299.29 to 299.46 K. Importantly, all of these values remained well below the adopted 358.15 K functional threshold, so the classification of the PGL case as a non-threshold case was unaffected by the investigated parameter variations.

For the 5 kW Fiber IPG YLS case at 100 m, the sensitivity of the predicted threshold time was more pronounced. A 25% reduction in either F_{cam} or α_s increased t_{lim} from 0.104 to 0.148 s, whereas a 25% increase reduced it to 0.080 s. Variations in μ produced a smaller effect, with t_{lim} ranging from 0.093 to 0.121 s. Nevertheless, the threshold continued to be reached for all parameter variations considered. These results indicate that uncertainty in the assumed camera optical parameters can noticeably affect the predicted quantitative response, particularly the threshold time under high-power irradiation, while the qualitative threshold classification of the two representative cases remained unchanged within the investigated ±25% sensitivity range. The selected variation range should be interpreted as an engineering sensitivity interval rather than as a statistically derived uncertainty or confidence interval.

3.8. Numerical ABS–Camera Comparison

Within the numerical three-dimensional analysis, the simulated 1.0 W, 1064 nm PGL-V-H-1064 laser produced markedly different predicted thermal responses in the two target models. At the simulated distance of 5 m, the ABS hotspot exceeded 373.15 K after 2.913 s, whereas the equivalent-camera model remained below 300 K and did not reach its 358.15 K threshold. These values refer exclusively to the numerical models and should not be interpreted as measurements obtained during the experimental campaign. The difference follows directly from the target-specific interaction model: ABS receives direct material absorption, whereas the equivalent camera includes the approximate lens–filter–sensor coupling factor.

Representative higher-power cases for both targets are summarized in Table 9. The comparison shows that identical laser conditions can produce substantially different maximum temperatures, threshold times, and fractions of the numerical domain above the adopted threshold, depending on the thermal and spectral properties assigned to the target.

Table 9. Representative three-dimensional cases for the ABS structural target and the equivalent-camera model.

Target	Scenario	T_{max} [K]	$\overline{T}$ [K]	t_{lim} [s]	f_{lim} [%]
ABS	Diode Lumics 300 W, 100 m	1070.77 †	334.01	0.274	12.46
ABS	Fiber IPG YLS 5 kW, 100 m	4630.56 †	573.34	0.005	30.55
ABS	Fiber Blue NUBURU 1.5 kW, 100 m	4443.65 †	592.09	0.003	35.93
Equivalent camera	PGL-V-H-1064, 1 W, 5 m	299.39	294.63	–	0.00
Equivalent camera	Diode Lumics 300 W, 100 m	638.52	310.31	5.845	8.44
Equivalent camera	Fiber IPG YLS 5 kW, 100 m	1548.73 †	398.18	0.104	25.38
Equivalent camera	Fiber Blue NUBURU 1.5 kW, 100 m	3105.76 †	608.04	0.005	58.27

† Very high terminal values of T_{max} are numerical severity indicators produced by continuation of the constant-property thermal model after threshold crossing. They should not be interpreted as physically realistic temperatures of an intact component. For these severe cases, t_{lim} is the primary physically meaningful quantity for comparison.

For the higher-power laser systems at 100 m, the comparison should focus primarily on threshold-crossing time rather than on the predicted terminal temperature. For the ABS target, the Diode Lumics 300 W, Fiber IPG YLS 5 kW, and Fiber Blue NUBURU 1.5 kW cases reached the adopted threshold after 0.274, 0.005, and 0.003 s, respectively. For the equivalent-camera model, the corresponding threshold times were 5.845, 0.104, and 0.005 s. These values provide a more meaningful basis for comparing severe irradiation cases because the constant-property formulation is no longer physically representative once substantial softening, degradation, melting, or other major material transformations have occurred. Accordingly, the very high T_{max} values marked in Table 9 should be interpreted only as numerical severity indicators. The comparison nevertheless shows a clear target-dependent response: the ABS model is dominated by direct material absorption and localized heating, whereas the equivalent-camera response is strongly influenced by the adopted spectral coupling. The quantities f_{lim} remain numerical-domain metrics and should not be interpreted as the physical percentage of a real component that has been damaged.

3.9. Experimental Results

The results presented from this point onward correspond exclusively to the exploratory experimental campaign. Unlike the preceding numerical analysis, these tests were performed with the PGL-V-H-1064 laser available in the laboratory and used laser–target distances between 0.5 and 6 m. The experimental observations should therefore not be interpreted as direct measurements of the numerical cases evaluated at 5, 10, 25, 50, and 100 m.

3.9.1. Individual FPV Cameras

The RunCam, BetaFPV, and Caddx Ratel 2 cameras were irradiated over distances from 0.5 to 6 m and exposure durations from 5 to 120 s. Temporary image perturbation compatible with dazzling or local saturation was observed during exposure. However, all three cameras recovered image acquisition after the laser was removed, and no permanent damage was observed either with the lenses installed or with the sensors directly exposed.

The absence of permanent damage is consistent with the combination of low source power, wavelength-dependent coupling of the optical assembly, and heat redistribution through the sensor package and electronic board. With the lens installed, part of the incident radiation may be reflected, scattered, or attenuated by optical elements and coatings. Conversely, removing the lens also removes its ability to concentrate the incident

radiation onto a smaller sensor region. The observations therefore support a distinction between reversible optical disruption and irreversible thermal damage.

3.9.2. Integrated Low-Cost Drone Camera

A different response was observed for the camera integrated into a low-cost foldable RC quadcopter marketed under the PQETBV brand (manufacturer: QUINDE), equipped with a camera advertised as supporting 1080p imaging. The retailer does not provide a specific model designation for the drone or identify the manufacturer and model of the internal camera module. No reliable manufacturer information was available for the camera-module part number, sensor format, lens type or focal length, presence or spectral characteristics of an IR-cut filter, or internal module dimensions. No suitable photograph of the internal camera module was obtained from the experimental campaign. Consequently, the failure mechanism cannot be attributed to a specific optical or sensor architecture, and the result is reported conservatively as a device-level observation. A persistent loss of image acquisition was observed following 120 s of irradiation at a laser–target distance of 3.0 m. The underlying physical failure mechanism could not be determined. The condition of the integrated camera before and after irradiation is shown in Figure 6.



(**a**) Before exposure.



(**b**) After exposure; permanently affected camera region.

Figure 6. Low-cost integrated drone camera before and after exposure to the PGL-V-H-1064 laser at a laser–target distance of 3.0 m and a total exposure duration of 120 s. Panel (**b**) shows the camera region associated with the observed permanent loss of image acquisition.

This contrast with the individual FPV cameras indicates that vulnerability cannot be generalized across camera types. Optical construction, filtering, internal geometry, sensor-to-lens spacing, thermal dissipation, and beam alignment can strongly modify the energy coupled to a sensitive region.

3.9.3. Optical Dazzling

Dazzling was observed in all cameras during laser exposure. The effect appeared as a temporary degradation of the acquired image, with partial or extensive loss of useful scene information while the beam was incident on the optical system or exposed sensor. In the three individual FPV cameras, normal image acquisition returned after exposure, demonstrating a reversible soft-kill effect without observable permanent sensor damage.

A representative example of the observed dazzling effect is shown in Figure 7.

This observation is important because the thermal camera model does not explicitly calculate pixel saturation, blooming, image contrast, or dazzling-spot size. Consequently, the experimental results confirm that temporary optical degradation can occur even when the modeled thermal threshold is not reached.



Figure 7. Representative image of dazzling observed with the integrated low-cost drone camera during the 3.0 m exposure sequence performed with the PGL-V-H-1064 laser. The total exposure duration of this sequence was 120 s. The image is used qualitatively to show the laser-affected image region and the associated loss of useful scene information during irradiation.

3.9.4. Structural Components

Localized thermal damage was also observed on structural components of the drone. The fairing exhibited a visible surface alteration after irradiation at 4.0 m for 90 s, whereas the propeller showed localized damage after exposure at 0.5 m for 20 s. The experimental record did not include a controlled measurement of the propeller rotational state during irradiation, and the damage initiation site was not documented with sufficient precision to distinguish unambiguously between the blade surface, hub, and blade-root region. The result is therefore reported conservatively as localized propeller damage rather than as a mechanism-specific failure of a particular propeller subregion. Representative images of both components are presented in Figure 8.



(**a**) Before exposure. (**b**) After exposure. (**c**) Propeller after exposure.

Figure 8. Experimental evidence of localized damage to structural drone components after exposure to the PGL-V-H-1064 laser: (**a**) fairing before exposure; (**b**) fairing after irradiation at 4.0 m for 90 s, showing the localized affected region; and (**c**) propeller after irradiation at 0.5 m for 20 s, showing the localized damaged region.

The consequences of the two exposures were not equivalent. In the fairing, the observed effect was primarily a localized surface alteration. In contrast, degradation of the propeller had a direct functional consequence, as the drone was subsequently unable to stabilize correctly in flight. This result illustrates that localized damage to a functionally critical component may impair UAV operation without requiring extensive damage to the overall airframe.

These observations are qualitatively consistent with the localized-heating behavior predicted by the three-dimensional thermal model. However, because the incident irradiance, beam diameter, and transient target temperature were not measured during the experimental tests, a direct point-by-point quantitative comparison between the numerical predictions and experimental observations is not possible. The structural experiments therefore provide qualitative experimental support for the predicted relevance of localized laser-induced heating and damage.

3.9.5. Experimental Summary and Numerical Comparison

A consolidated summary of the experimental configurations, exposure conditions, and observed reversible and permanent effects is provided in Table 10.

Table 10. Summary of the experimental tests performed with the PGL-V-H-1064 laser, explicitly distinguishing reversible soft-kill effects from permanent or structural damage.

Target/Configuration	Distance	Exposure	Reversible Soft-Kill	Permanent/Structural Damage	Observed Outcome
RunCam, BetaFPV, Caddx Ratel 2; lens installed	0.5–6 m	5–120 s	Yes	No	Temporary dazzling/saturation followed by recovery after exposure.
RunCam, BetaFPV, Caddx Ratel 2; sensor exposed	0.5–6 m	5–120 s	Yes	No	Temporary optical perturbation was observed; image acquisition recovered and no permanent damage was identified.
Integrated low-cost drone camera	3.0 m	120 s	No *	Yes	Dazzling occurred during irradiation, followed by permanent loss of image acquisition.
Drone fairing; direct incidence	4.0 m	90 s	N/A	Yes	Localized thermal/surface damage.
Drone propeller; direct incidence	0.5 m	20 s	N/A	Yes	Localized damage followed by loss of flight stabilization.

* Dazzling was observed during irradiation of the integrated low-cost camera, but because the unit subsequently suffered permanent failure, this outcome is not classified as a reversible soft-kill result. "N/A" indicates that the soft-kill classification is not applicable to structural components.

The observations were qualitatively consistent with several numerical trends. The lack of permanent damage in the individual cameras agrees with the equivalent-camera simulations in which the PGL-V-H-1064 laser did not reach the adopted thermal functional threshold at any simulated distance. At the same time, the experimentally observed dazzling demonstrates a functional optical effect that lies outside the thermal model.

The structural tests also provide qualitative support for the predicted importance of beam concentration and dwell time. The three-dimensional ABS model produced localized hotspots and crossed the adopted ABS threshold only under the most concentrated PGL condition. The experimental fairing damage was observed after 90 s of exposure at 4.0 m, whereas localized propeller damage was observed after 20 s at 0.5 m. Because incident irradiance and temperature were not measured during the experiments, this comparison remains qualitative and does not constitute a point-by-point quantitative comparison between predicted and measured quantities.

4. Discussion

4.1. Why a Multiscale Modeling Strategy Is Useful

The three modeling levels answer different but complementary questions. The lumped model provides a computationally inexpensive way to screen a large parameter space and identify general trends across lasers, targets, and distances. Its principal limitation is the assumption of a uniform temperature in an effective illuminated volume. A localized laser source can violate this assumption even when the classical Biot-number criterion is favorable.

A further limitation of the lumped formulation arises from the definition of the effective heated area. As the beam expands with distance, the model associates the illuminated

area with the corresponding effective thermal mass. For a real component of finite dimensions, however, part of the beam may no longer intercept the target once the beam diameter becomes comparable to or larger than the component itself. Consequently, long-range lumped predictions should be interpreted primarily as screening estimates rather than as exact representations of finite-target energy coupling.

The three-dimensional model resolves this limitation by directly representing hotspot formation and heat diffusion. The ABS results demonstrate that local maximum temperature can exceed a material threshold while the domain-average temperature remains much lower. Thus, relying on average temperature alone can underestimate localized thermal vulnerability.

The equivalent-camera model adds another level of differentiation. A camera should not be treated simply as a silicon slab because the incident radiation interacts with lenses, filters, coatings, microlenses, packaging, and electronics before and after reaching the photosensitive region. The present model represents only the global thermal consequence of this optical stack through approximate effective factors. Nevertheless, the strong difference between the ABS and camera responses to the same 1064 nm source demonstrates the need for target-specific coupling.

4.2. Soft-Kill Versus Hard-Kill Interpretation

The numerical results should not be used to claim that a camera is optically blinded whenever its thermal threshold is crossed, nor that it is unaffected whenever the threshold is not crossed. Optical dazzling and saturation can occur at energy levels below those required for permanent thermal damage [7,8,10]. This distinction was directly observed in the experiments: all tested cameras exhibited temporary dazzling, whereas the RunCam, BetaFPV, and Caddx Ratel 2 units recovered after exposure and showed no observable permanent damage. Thus, the 1 W camera simulations and experiments are mutually consistent at a qualitative level: failure to reach the thermal threshold does not preclude a reversible soft-kill effect.

The integrated low-cost drone camera provides an important counterexample to any universal camera response. It suffered permanent damage after 120 s at 3.0 m, showing that camera-specific optics, filtering, thermal paths, geometry, and beam alignment can strongly modify vulnerability. The equivalent-camera model should therefore be interpreted as a reference thermal representation rather than a predictor for every commercial camera architecture.

For structural components, crossing a polymer glass-transition-related threshold indicates a condition compatible with softening, deformation, or local stiffness reduction; it does not by itself prove complete perforation or loss of flight capability. Nevertheless, the experiments showed that localized damage can have an operational consequence: damage to the propeller was followed by loss of flight stabilization. Previous work likewise indicates that functional failure may precede complete material removal [6,11–13].

4.3. Influence of Power, Beam Quality, Distance, and Wavelength

Across the simulations, nominal power was only one contributor to effectiveness. Increasing power generally reduced threshold time, but beam quality and initial diameter determined how strongly the energy remained concentrated at range. Distance increased the effective beam radius and reduced peak irradiance. In the three-dimensional cases, atmospheric attenuation and the simplified turbulence broadening provided additional losses.

The equivalent-camera results further show that spectral coupling can reverse an ordering based solely on nominal power. Within the adopted assumptions, the 1.5 kW blue laser crossed the camera threshold substantially faster than the 5 kW near-infrared laser at 100 m because the blue band was assigned a much larger effective coupling factor. This result should be

viewed as a sensitivity demonstration rather than an experimentally calibrated prediction, because measured transmission and sensor-response curves were not available.

4.4. Relationship to Previous Work

The observed importance of beam concentration and pointing stability is consistent with previous C-UAS studies that identify acquisition, tracking, and pointing performance as critical to delivered irradiance [14,31]. The distinction between reversible optical disruption and permanent damage is also consistent with experimental studies of CMOS dazzling and laser-induced UAV sensor effects [7,8,10]. Furthermore, the predicted vulnerability of polymers and electronics relative to more thermally resistant metallic structures is qualitatively consistent with literature on directed-energy interaction with composite and flight-control components [11–13].

The main contribution of the present framework is not a new fundamental heat-transfer equation, but the integration of uniform screening, spatial thermal modeling, approximate spectral coupling, and a preliminary laser-source cost comparison under a single numerical workflow. This provides a reproducible basis for selecting scenarios for targeted experiments rather than attempting exhaustive testing over every possible laser–target combination.

4.5. Model Limitations

Several limitations constrain quantitative interpretation. First, material properties are treated as constant within each simulation, even after temperatures exceed the ranges in which softening, decomposition, carbonization, melting, ablation, or other major physical transformations would occur. Consequently, predicted terminal temperatures above approximately 1000 K, and particularly values reaching several thousand kelvin, fall well outside the regime in which the constant-property representation can be considered physically realistic. Such values are retained only as numerical indicators of severe energy deposition and should not be interpreted as temperatures that an intact component would actually reach. For these severe irradiation cases, the threshold-crossing time t_{lim} is therefore emphasized as the more physically meaningful model output.

A further limitation concerns the definition of the thermal and functional thresholds. Because the adopted values correspond to different physical phenomena, threshold crossing does not have the same meaning for all targets. In addition, material grade, composition, manufacturing process, environmental condition, and device architecture can shift the actual temperature at which softening, functional degradation, or permanent failure occurs. The reported threshold times and success rates are therefore conditional on the criteria defined in Table 2 and should be interpreted primarily as comparative vulnerability indicators rather than universal damage temperatures or failure probabilities.

Second, the wavelength dependence of absorption is represented through effective band factors rather than measured spectral properties of specific samples. The camera is likewise represented by a homogeneous thermal equivalent and does not resolve optical focusing, interfacial reflection, lens coatings, microlenses, or pixel-level photoelectric behavior.

Third, the three-dimensional grid does not fully resolve the absorption depth in every scenario. Threshold times of only a few numerical steps should therefore be interpreted as orders of magnitude. Full grid-independence testing remains necessary for the most severe cases.

Fourth, irradiation is assumed to be continuous, normally incident, centered, and stable. A real engagement would include target motion, jitter, platform vibration, atmospheric variability, aiming error, and potentially time-varying range. These effects can reduce effective dwell time and spread energy over a larger target area.

Finally, the preliminary source-cost comparison includes estimated laser-source acquisition prices only. It excludes acquisition and tracking sensors, beam directors, optical trains, power supply, cooling, stabilization, integration, maintenance, training, operating costs, and other system-level expenditures. Accordingly, the ranking is a screening-level source-cost comparison and must not be interpreted as a complete C-UAS cost-effectiveness analysis or as a basis for procurement decisions.

The experimental campaign also has important limitations. It was exploratory, the beam was aligned manually, and no direct measurements were made of target-plane power, beam diameter, irradiance, transient temperature, or spatial energy distribution. In addition, systematic replicate trials under identical irradiation conditions were not performed. The selected camera tests conducted after removal of the optical assembly corresponded to different experimental configurations and should not be interpreted as statistical repetitions. Consequently, repeatability, experimental variance, and confidence intervals could not be quantified. The experimental observations should therefore be interpreted as qualitative evidence supporting the distinction between reversible dazzling, permanent camera damage, and localized structural damage, rather than as statistically validated performance limits.

4.6. Numerical–Experimental Relationship

The exploratory campaign complements the thermal models by testing phenomena that are not explicitly represented numerically. The most important example is dazzling: it was observed experimentally in every camera despite the fact that the PGL-V-H-1064 laser did not reach the equivalent-camera thermal threshold. This supports the methodological separation between optical soft-kill and thermal failure.

The absence of permanent damage in the individual FPV cameras is qualitatively compatible with the low temperature rise predicted by the equivalent-camera model for the PGL-V-H-1064 laser. The permanent damage observed in the integrated low-cost camera, however, also demonstrates the limits of a homogeneous equivalent representation and highlights the influence of device-specific optics and thermal design.

For structural targets, the observation of localized fairing and propeller damage is consistent with the model prediction that the PGL-V-H-1064 laser can produce strongly localized heating when the beam remains sufficiently concentrated. The comparison should not be interpreted quantitatively because the experimental incident irradiance, spot diameter, and transient temperature were not measured. The experiments therefore provide qualitative experimental support for the main modeled trends rather than a calibration or point-by-point confirmation of the numerical predictions.

5. Conclusions

A multiscale framework was developed to evaluate continuous-wave laser interaction with representative UAV components using a lumped screening model, a three-dimensional structural-material model, a dedicated equivalent-camera model, and an exploratory experimental campaign.

The lumped analysis evaluated 1350 laser–material–distance combinations and reached the prescribed thermal or functional threshold in 85.0% of cases. The numerical checks showed an energy-balance residual of approximately 1.55×10^{-11}% and time-step differences below 0.002%. The results confirmed that distance, beam expansion, target thermal properties, and threshold definition strongly affect the predicted response and that nominal laser power alone is insufficient for comparing systems.

The three-dimensional models revealed strongly localized heating. For ABS, the adopted 373.15 K threshold was reached in 76 of 80 cases. The PGL-V-H-1064 laser crossed

this threshold only at 5 m, after approximately 2.913 s. For the equivalent camera, the 358.15 K functional threshold was reached in 75 of 80 cases, while the PGL-V-H-1064 laser remained below the threshold at all five simulated distances. The contrast between the ABS and camera responses demonstrates the need to treat direct laser–material interaction separately from energy coupling through an optical–electronic assembly.

These numerical success rates and threshold times are conditional on the target-specific criteria adopted in this study. In particular, crossing the ABS threshold indicates entry into a polymer glass-transition/softening regime, whereas crossing the equivalent-camera threshold indicates attainment of a functional thermal criterion. These events therefore represent different physical effects and should not be interpreted as equivalent measures of permanent destruction.

The experiments clarified the distinction between optical soft-kill and permanent damage. All tested cameras exhibited dazzling during irradiation. However, the individual RunCam, BetaFPV, and Caddx Ratel 2 cameras recovered after exposure and showed no observable permanent damage, including in tests with the sensor exposed. In contrast, the camera integrated in a low-cost drone suffered permanent damage after a 120 s exposure at 3.0 m. These results show that a thermal model may correctly indicate low permanent-damage potential for a reference camera while temporary optical disruption can still occur, and that vulnerability varies significantly between camera architectures.

Localized structural damage was also obtained experimentally. The drone fairing showed visible damage after exposure at 4.0 m for 90 s, and the propeller was damaged after 20 s at 0.5 m. The latter produced a direct functional consequence because the drone subsequently failed to stabilize correctly in flight. This observation illustrates that functional neutralization can result from damage to structural or propulsion components without requiring complete destruction of the airframe.

The numerical results indicate that the predicted thermal response depends on several interacting parameters, including source power, beam characteristics, distance, wavelength-dependent coupling, and exposure duration. The exploratory experimental observations illustrate possible optical and structural effects but do not allow the individual contributions of these parameters to be quantified.

Author Contributions: Conceptualization, J.S.S. and D.S.; methodology and software, D.R.; validation and formal analysis, D.R., J.S.S., D.S.; resources, D.R., J.S.S., D.S., J.A., D.L. and P.M.d.S.; writing—original draft preparation, D.R.; writing—review and editing, D.R., J.S.S., D.S., J.A., D.L. and P.M.d.S.; supervision, J.S.S. and D.S.; funding acquisition, J.S.S. and P.M.d.S. All authors have read and agreed to the published version of the manuscript.

Funding: This research was supported by the Military Academy Research Center (CINAMIL).

Institutional Review Board Statement: Not applicable.

Informed Consent Statement: Not applicable.

Data Availability Statement: The numerical simulation outputs and processed data supporting the tables and figures are available from the corresponding author upon request. Experimental photographs, video recordings, and related observations may also be provided upon request, subject to applicable institutional and security restrictions. No public data repository has been established for this study.

Acknowledgments: The authors would like to acknowledge Military Academy Research Center (CINAMIL); the Physics Department of NOVA School of Science and Technology, NOVA University Lisbon; and the Department of Physics of Instituto Superior Técnico, University of Lisbon, for their support and contributions to this work. ChatGPT (OpenAI) was used for language refinement, grammatical correction and editorial support. All AI-assisted content was reviewed by the authors, who take full responsibility for the final manuscript.

Conflicts of Interest: The authors declare no conflicts of interest.

Abbreviations

The following abbreviations are used in this manuscript:

ABS	Acrylonitrile butadiene styrene
ATP	Acquisition, tracking, and pointing
CFRP	Carbon-fiber-reinforced polymer
CMOS	Complementary metal-oxide-semiconductor
C-UAS	Counter-unmanned aerial system
FR4	Flame Retardant 4
HEL	High-energy laser
IR	Infrared
NIR	Near infrared
UAV	Unmanned aerial vehicle

Appendix A. Laser Input Parameters

The main laser parameters used as simulation inputs are listed in Table A1.

Table A1. Physical, optical, and economic laser input parameters used in the simulations.

Laser	λ [nm]	P [W]	M^2	D_0 [mm]	η_{opt}	Price [EUR]
Fiber IPG YLR 500 W	1070	500	1.2	6	0.90	38,000
Fiber IPG YLR 1 kW	1070	1000	1.3	6	0.90	72,000
Fiber IPG YLR 2 kW	1070	2000	1.5	7	0.90	120,000
Fiber IPG YLS 3 kW	1070	3000	1.6	8	0.88	165,000
Fiber IPG YLS 5 kW	1070	5000	2.0	10	0.88	260,000
Diode Lumics 300 W	808	300	5.0	10	0.85	14,000
Diode Lumics 500 W	808	500	6.0	12	0.85	20,000
Diode Lumics 1 kW	808	1000	8.0	15	0.85	32,000
Diode DILAS 2 kW	808	2000	10.0	20	0.85	52,000
DPSS Coherent Verdi 200 W	532	200	2.0	4	0.80	48,000
DPSS Coherent Verdi 500 W	532	500	2.2	5	0.80	95,000
DPSS Lumentum 1 kW	532	1000	2.5	6	0.80	165,000
Fiber Blue NUBURU 400 W	445	400	1.4	5	0.70	62,000
Fiber Blue NUBURU 800 W	445	800	1.6	6	0.70	115,000
Fiber Blue NUBURU 1.5 kW	445	1500	1.8	7	0.70	195,000
PGL-V-H-1064 1 W	1064	1	1.1	1.5	1.00	–

Target Material Parameters

The principal thermal, optical, and geometric properties adopted for the representative UAV targets are summarized in Tables A2 and A3. These parameters correspond to the equivalent materials used in the numerical models and are not intended to represent the complete variability of commercial UAV components.

Table A2. Thermal and geometric properties adopted for the representative UAV targets.

Target/Material	ρ [kg m^{-3}]	c_p [J kg^{-1} K^{-1}]	k [W m^{-1} K^{-1}]	h_m [mm]
ABS fairing	1050	1400	0.18	2.0
Polycarbonate fairing	1200	1250	0.20	2.0
Glass-fiber-reinforced nylon	1350	1000	0.30	3.0
CFRP structural arm	1600	900	0.60	4.0
Aluminum structure	2700	900	205	1.5

Table A2. *Cont.*

Target/Material	ρ [kg m^{-3}]	c_p [J kg^{-1} K^{-1}]	k [W m^{-1} K^{-1}]	h_m [mm]
Magnesium structure	1800	1020	160	1.5
Stainless-steel shaft	8000	500	16	3.0
FR4 electronic board	1850	1100	0.30	1.6
Silicon sensor	2330	700	148	0.5
Optical-glass lens	2500	750	1.10	1.5
Equivalent camera	2210.41	862.03	0.565	2.45

Table A3. Threshold and effective optical and boundary parameters adopted for the representative UAV targets.

Target/Material	T_{lim} [K]	α_s	μ [m^{-1}]	ε
ABS fairing	373.15	0.60	2.0×10^4	0.90
Polycarbonate fairing	423.15	0.75	3.0×10^4	0.90
Glass-fiber-reinforced nylon	443.15	0.70	2.0×10^4	0.85
CFRP structural arm	450.15	0.65	1.5×10^4	0.85
Aluminum structure	933.15	0.20	1.0×10^5	0.20
Magnesium structure	923.15	0.25	8.0×10^4	0.30
Stainless-steel shaft	1700.15	0.35	1.0×10^5	0.40
FR4 electronic board	403.15	0.85	4.0×10^4	0.90
Silicon sensor	398.15	0.65	1.0×10^5	0.70
Optical-glass lens	820.15	0.10	5.0×10^2	0.90
Equivalent camera	358.15	0.50	2.5×10^4	0.85

The listed α_s and μ values correspond to the baseline material properties. In the three-dimensional models, wavelength-dependent effective values were obtained using the spectral factors defined for each wavelength band and target class. The values of T_{lim} are target-specific screening criteria and do not represent an identical physical failure mechanism across all materials. Their individual physical interpretations and supporting rationale are summarized in Table 2.

References

1. Chauhan, D.; Kagathara, H.; Mewada, H.; Patel, S.; Kavaiya, S.; Barb, G. Nation's Defense: A Comprehensive Review of Anti-Drone Systems and Strategies. *IEEE Access* **2025**, *13*, 53476–53505. [CrossRef]
2. Branco, B.; Silva, J.S.S.; Correia, M. Cyber Attacks on Commercial Drones: A Review. *IEEE Access* **2025**, *13*, 9566–9577. [CrossRef]
3. Branco, B.; Silva, J.S.; Correia, M. D3S: A Drone Security Scoring System. *Information* **2024**, *15*, 811. [CrossRef]
4. Zidane, Y.; Silva, J.S.; Tavares, G. Jamming and Spoofing Techniques for Drone Neutralization: An Experimental Study. *Drones* **2024**, *8*, 743. [CrossRef]
5. Kaushal, H.; Kaddoum, G. Applications of Lasers for Tactical Military Operations. *IEEE Access* **2017**, *5*, 20736–20753. [CrossRef]
6. Chaari, M.Z.; Al-Maadeed, S. Testing the Efficiency of Laser Technology to Destroy Rogue Drones. *Secur. Def. Q.* **2020**, *32*, 31–38. [CrossRef]
7. Wang, X.; Xu, Z.; Zhong, H.; Cheng, X.A.; Xing, Z.; Zhang, J. Fresnel Diffraction Model for Laser Dazzling Spots of Complementary Metal Oxide Semiconductor Cameras. *Sensors* **2024**, *24*, 5781. [CrossRef] [PubMed]
8. Fjellström, J. Laser Dazzling of CMOS Imaging Sensors Using Amplitude Modulated and Continuous Wave Lasers. Master's Thesis, Department of Physics, Umeå University, Umeå, Sweden, 2023.
9. Kuantama, E.; Zhang, Y.; Rahman, F.; Han, R.; Dawes, J.; Mildren, R.; Abir, T.A.; Nguyen, P. Laser-Based Drone Vision Disruption with a Real-Time Tracking System for Privacy Preservation. *Expert Syst. Appl.* **2024**, *255*, 124626. [CrossRef]
10. Wu, J.; Huang, S.; Wang, X.; Kou, Y.; Yang, W. Study on the Performance of Laser Device for Attacking Miniature UAVs. *Optics* **2024**, *5*, 378–391. [CrossRef]
11. Liu, L.; Xu, C.; Cai, S.; Wang, J.; Huang, D.; Yang, K.; Zheng, C.; Guo, J. Research on the Damage Characteristics of a UAV Flight Control System Irradiated by a Continuous Laser. *Aerospace* **2025**, *12*, 161. [CrossRef]
12. Zhang, Y.X.; Zhu, Z.; Joseph, R.; Shihan, I.J. Damage to Aircraft Composite Structures Caused by Directed Energy System: A Literature Review. *Def. Technol.* **2021**, *17*, 1269–1288. [CrossRef]

13. Siora, O.; Lukashenko, V.; Bernatskyi, A. An Interdisciplinary Study of the Effect of Laser Radiation on Carbon Fiber-Reinforced Polymer, in the Context of Counteracting Unmanned Aerial Vehicles. *Hist. Sci. Technol.* **2025**, *15*, 195–215. [CrossRef]
14. Ye, Z.; You, J.; Gu, J.; Kou, H.; Li, G. Modeling and Simulation of Urban Laser Countermeasures Against Low-Slow-Small UAVs. *Drones* **2025**, *9*, 419. [CrossRef]
15. Hu, H.; Peng, X.; He, X.; Guo, X. Infield Simulation and Testing Method of ATP in Laser Anti-UAV System. *J. Phys. Conf. Ser.* **2025**, *2988*, 012004. [CrossRef]
16. Liu, W.; Zhang, L.; Wang, W.; Zhang, M.; Zhang, J.; Gao, F.; Zhang, B. Damage Capability of Laser System in Ground-Air Defense Environments. *Chin. J. Aeronaut.* **2025**, *38*, 103625. [CrossRef]
17. Liu, L.; Xu, C.; Zheng, C.; Cai, S.; Wang, C.; Guo, J. Vulnerability Assessment of UAV Engine to Laser Based on Improved Shotline Method. *Def. Technol.* **2024**, *33*, 588–600. [CrossRef]
18. Veerabuthiran, S.; Paul, S.; Nayak, J. Investigation of the CMOS Sensor Disruption Induced by a Nanosecond Single Pulse Laser at 1064 nm. *Optik* **2026**, *348*, 172698. [CrossRef]
19. Song, H.; Obara, E.; Zhu, L.; Han, Z.; Sun, B.; Feng, Y.; Luo, C. Damage Mechanism and Residual Tensile Strength of CFRP Laminates Subjected to Continuous Laser Irradiation. *Opt. Laser Technol.* **2026**, *199*, 115083. [CrossRef]
20. Zhang, B.; Kim, C.; Li, W.; Chirinos, J.; Mao, X.; Harrison, R.; Zorba, V. Towards Robust Laser Beam Propagation in Atmospheric Turbulence. *Photonics Res.* **2026**, *14*, 3245–3267. [CrossRef]
21. Gamaly, E.G.; Rode, A.V. Physics of Ultra-Short Laser Interaction with Matter: From Phonon Excitation to Ultimate Transformations. *Prog. Quantum Electron.* **2013**, *37*, 215–323. [CrossRef]
22. Jürgens, P.; Garcia, C.L.; Balling, P.; Fennel, T.; Mermillod-Blondin, A. Diagnostics of fs Laser-Induced Plasmas in Solid Dielectrics. *Laser Photonics Rev.* **2024**, *18*, 2301114. [CrossRef]
23. Incropera, F.P.; DeWitt, D.P.; Bergman, T.L.; Lavine, A.S. *Fundamentals of Heat and Mass Transfer*, 6th ed.; John Wiley & Sons: Hoboken, NJ, USA, 2007.
24. Çengel, Y.A.; Ghajar, A.J. *Heat and Mass Transfer: Fundamentals & Applications*, 5th ed.; McGraw-Hill Education: New York, NY, USA, 2015.
25. Li, J.; Jia, Y.; Li, T.; Zhu, Z.; Zhou, H.; Peng, X.; Jiang, S. Tensile Behavior of Acrylonitrile Butadiene Styrene at Different Temperatures. *Adv. Polym. Technol.* **2020**, *2020*, 8946591. [CrossRef]
26. Covestro. *Makrolon 3107: ISO Datasheet*; Edition 01.09.2015; Covestro AG: Leverkusen, Germany, 2015. Available online: https://www.sentezkimya.com/documents-en/pc-polycarbonate/PC%20-%20COVESTRO%20-%20Makrolon%203107%20-%20TDS%20f.pdf (accessed on 22 October 2026).
27. Matrix USA Inc. *KB-6160A FR-4 Copper Clad Laminates*; Technical Datasheet; Revision 16 June 2020; Matrix USA Inc.: Santa Clara, CA, USA, 2020. Available online: https://www.matrixelectronics.com/wp-content/uploads/2022/07/KB-6160A_TDS.pdf (accessed on 22 October 2026).
28. onsemi. *MT9P031: 1/2.5-Inch 5 MP CMOS Digital Image Sensor*; Technical data sheet; storage-temperature range up to 125 °C; onsemi: Scottsdale, AZ, USA, 2025.
29. SCHOTT AG. *N-BK7 Optical Glass Data Sheet*; Technical data sheet; transformation temperature $T_g = 557$ °C; SCHOTT AG: Mainz, Germany, 2015.
30. Hamamatsu Photonics. *S13101 CMOS Area Image Sensor*; Technical data sheet; operating-temperature range up to 85 °C; Hamamatsu Photonics: Shizuoka, Japan, 2022.
31. Selvamuthu, D.; Badiyasara, H.; Tripathia, S.; Kalitab, P.; Rajc, R. Reliability Analysis of an Anti-Drone System by Considering Random Environmental Factors. *Reliab. Theory Appl.* **2024**, *19*, 186–205. [CrossRef]

Disclaimer/Publisher's Note: The statements, opinions and data contained in all publications are solely those of the individual author(s) and contributor(s) and not of MDPI and/or the editor(s). MDPI and/or the editor(s) disclaim responsibility for any injury to people or property resulting from any ideas, methods, instructions or products referred to in the content.